

Feasibility analysis of a proposed test of quantum gravity via novel optical magnetometry in xenon

J. Maldaner,^{1,*} M. Fridman,² S. Das,² and G. Porat^{1,3,†}

¹*Department of Physics, University of Alberta, Edmonton, Alberta T6G 2E1, Canada*

²*Department of Physics and Astronomy, University of Lethbridge, Lethbridge, Alberta T1K 3M4, Canada*

³*Department of Electrical and Computer Engineering,
University of Alberta, Edmonton, Alberta T6G 1H9, Canada*

(Dated: February 28, 2024)

We present an analysis of the sensitivity limits of a proposed experimental search for quantum gravity, using a novel approach based on optical magnetometry in the noble gas isotope ^{129}Xe . The analysis relies on a general uncertainty principle model that is consistent with most formulations of quantum gravity theory, where the canonical uncertainty relations are modified by a leading-order correction term that is linear in momentum. In turn, this correction modifies the magnetic moment of the spin-polarized ^{129}Xe atoms that are immersed in a magnetic field in the proposed experiment, which results in a velocity-dependent variation of their Larmor frequency, that is detected via two-photon laser spectroscopy. The thermal distribution of atomic velocities, in conjunction with the Doppler effect, is used to scan the interrogating laser over different atomic velocities, and search for a corresponding variation in their Larmor frequencies. We show that the existing bounds on the leading-order quantum gravity correction can be improved by 10^7 with existing technology, where another factor of 10^2 is possible with near-future technical capabilities.

I. INTRODUCTION

Quantum gravity (QG), the union of general relativity and quantum mechanics, is one of the most fundamentally significant outstanding problems in theoretical physics. The study of QG has resulted in a number of distinct proposed formulations including superstring theory, loop quantum gravity, and doubly special relativity, to name a few [1, 2]. The generalized uncertainty principle (GUP) is consistent with all the above forms of QG theory and predicts modifications in several areas of quantum mechanics, allowing for experimental searches for QG effects without the need to conform to a specific formulation [3, 4]. While most GUP formulations consider only a correction that is quadratic in momentum, recently a more general model has been developed, which includes both linear and quadratic corrections [3, 5]. For example, in one dimension, the GUP is given by

$$\Delta x \Delta p \geq \frac{\hbar}{2} \left[1 - 2 \frac{\alpha_0}{M_p c} \langle p \rangle + 4 \frac{\beta_0}{M_p^2 c^2} \langle p^2 \rangle \right], \quad (1)$$

where x is position, p is momentum, α_0 and β_0 are the linear and quadratic dimensionless GUP parameters, respectively, c is the speed of light, and $M_p = \sqrt{\hbar c / G}$ is the Planck mass, where \hbar is the reduced Planck's constant, G is the gravitational constant, and $M_p c$ is the Planck momentum.

The GUP parameter α_0 defines a minimum possible length $\ell_{min} \propto \alpha_0 \ell_P$, where $\ell_P = \sqrt{\hbar G / c^3}$ is the Planck length. It is generally agreed that ℓ_{min} must be between

the Planck length $\ell_P \sim 10^{-35}\text{m}$ and the electroweak length $\ell_{EW} \sim 10^{-18}\text{m}$ [6, 7], where the latter is the scale in which the Large Hadron Collider operates and in which no minimum length has been observed [8]. This places the commonly agreed upon upper bound of the linear GUP parameter at $\alpha_0 \leq 10^{17}$. As for the quadratic correction term, different methods have placed experimental upper bounds on β_0 , ranging from 10^{21} to 10^6 [6, 9–11].

This paper is published in conjunction with the paper by Fridman et al. [12], which analyzes the effects of the linear and quadratic GUP corrections on the nuclear magnetic moment of an atom, and outlines an experiment for detecting these effects through Larmor frequency measurements in a novel optical magnetometer utilizing direct (ultraviolet) optical access to atomic transitions in the ^{129}Xe noble gas atom. An optical magnetometer measures the spin precession frequency of an ensemble of spin-polarized atoms, i.e., the Larmor frequency. Without QG correction, this frequency is given by $\omega_{B,0} = \gamma B$, where γ is the gyromagnetic ratio of the atom and B is the magnetic field strength. When the GUP QG correction is introduced and we include corrections up to the $\mathcal{O}(m^2 v^2)$ term, the Larmor frequency becomes $\omega_B(v) = \omega_{B,0} (1 - \alpha_0 m v / M_p c + \beta_0 m^2 v^2 / M_p^2 c^2)$, where m is the atom's mass and v is the atom's velocity [2]. Therefore, if the Larmor frequency in an optical magnetometer is experimentally shown to depend on the velocity of the magnetometer's atoms, it will be an indication of QG effects. Conversely, if no dependence is shown, the measurement's sensitivity can set upper bounds on α_0 and β_0 .

Here, we carry out an analysis of the sensitivity limits of the proposed experiment. We consider a thermal atomic ensemble and include only the first-order correction term parameterized by α_0 and neglect β_0 , for the following reasons. First, even if an ensemble of oganesson

* maldaner@ualberta.ca

† gporat@ualberta.ca

atoms, the heaviest discovered element, is at room temperature, the ratio of the most probable momentum (in a Boltzmann-Mawell distribution [13]) of such atoms to the Planck momentum is $mv/M_p c = \sqrt{2m_{294\text{Og}}k_B T}/M_p c \sim 10^{-23}$, where $m_{294\text{Og}}$ is the mass of oganesson, k_B is Boltzmann's constant, and $T = 300\text{K}$ is room temperature. Therefore, as long as $\beta_0/\alpha_0 \ll 10^{23}$ the quadratic component in Eq. 2 can be neglected. Given that the existing bounds on β_0 range from 10^{21} to 10^6 , the quadratic component is negligible at least for $\alpha_0 > 10^{-2}$, and possibly even for $\alpha_0 > 10^{-17}$. Hence, there is a wide range of possible values of interest of α_0 , i.e. $10^{-2} < \alpha_0 < 10^{17}$, where the quadratic term is negligible. Therefore, henceforth we denote the QG correction

$$\mathcal{C}(v) = \alpha_0 \frac{mv}{M_p c}, \quad (2)$$

so that the QG-corrected Larmor frequency is

$$\omega_B(v) = \omega_{B,0} (1 - \mathcal{C}(v)). \quad (3)$$

In our analysis, we consider existing or near-future technological capabilities, where we propose measuring the QG-induced Larmor frequency variation across the velocity distribution of a thermal ensemble of hyperpolarized ^{129}Xe atoms via two-photon optical magnetometry, with some similarity to the magnetometer proposed by Altieri et al. [14]. In section II we detail the experimental methodology and derive the signal and noise models of the optical magnetometry experiment. In section III we outline the state of the art in magnetic field uniformity, deep ultraviolet (DUV) laser power and frequency stability, and techniques to maximize the spin polarization decay time of ^{129}Xe . We use these data to constrain experimental parameters in our model. Finally, in section IV, we optimize the values of the remaining unconstrained experimental parameters, calculate the corresponding sensitivity and bound on α_0 , and discuss the results, where we also consider and reasonable extrapolations of technical capabilities. Our analysis shows that it is feasible for this method's sensitivity to reveal QG signatures corresponding to $\alpha_0 \gtrsim 10^9$ with existing technology, where key factors are a high-power, tunable CW or high pulse repetition rate frequency comb laser in the DUV, and a high degree of spatial uniformity of the magnetic field.

II. PROPOSED EXPERIMENTAL METHODOLOGY AND SENSITIVITY ESTIMATION

A. Experimental Methodology

The principle of our proposed experiment is illustrated in Fig. 1 and follows the general principles of optical magnetometers [15]. We assume a hyperpolarized atomic gas of ^{129}Xe atoms, i.e., where the atoms are in the same

magnetic sublevel of the ground state. These atoms are placed in a magnetic field that is perpendicular to their spin orientation, i.e., perpendicular to the quantization axis used in the energy level diagram depicted in Fig. 1 (a). Therefore, the collective atomic spin precession about the magnetic field is manifested as a coherent oscillation of the atomic state between the ground state's two magnetic sublevels, at the Larmor frequency. An ultraviolet laser beam, with σ^+ circular polarization and wavelength of 256 nm, propagates through the gas in a direction perpendicular to the magnetic field. This laser light drives a two-photon transition from the ground state $m = -1/2$ sublevel to the $5p^5(^2P_{3/2})_6P^2[\frac{5}{2}]_2, m = +3/2$ excited state. Note that, under these conditions, there is no dipole-allowed two-photon transition from the ground state $m = +1/2$ sublevel. Therefore, since the atomic population of the ground state $m = -1/2$ sublevel oscillates at the Larmor frequency, so does the excited population. The excited atoms then decay to either the $5p^5(^2P_{3/2})_6S^2[\frac{3}{2}]_1$ or $5p^5(^2P_{3/2})_6S^2[\frac{3}{2}]_2$ state, by emitting near-infrared (NIR) radiation, before decaying back to the ground state. Hence, the amplitude of the NIR radiation follows the excited population and oscillates at the Larmor frequency. In our experiment, the NIR radiation is detected and the resulting signal is analyzed for extracting the Larmor frequency, which carries information on the QG correction as expressed by Eqs. 2 and 3.

The variation in the Larmor frequency, ω_B , depends on the velocity of the xenon atoms, with greater velocity producing a greater shift. Therefore, identical atoms must be traveling at different velocities through the same magnetic field to produce different shifts of their Larmor frequency, for these shifts to be detected. Atoms in a thermal ensemble move with a wide range of velocities, described by the Maxwell-Boltzmann distribution. Due to the atoms' motion, their transition resonance frequencies are Doppler shifted, resulting in a Gaussian distribution of resonance frequencies that is broader than the natural linewidth [13]. When sweeping the laser frequency across the Doppler broadened profile, where the laser linewidth is much smaller than the Doppler width, xenon atoms with the corresponding velocity are excited (see Fig. 1 (c)). The relationship between the laser angular frequency ω_l in the lab frame of reference, the resonant angular frequency ω_{Xe} in the xenon atom's frame of reference, and the atom's velocity v is [16]

$$v(\omega_l) = c \left(1 - \frac{\omega_{\text{Xe}}}{\omega_l} \right). \quad (4)$$

As the laser probes atoms with different velocities, this corresponds to different values of $\mathcal{C}(\omega_l) = \mathcal{C}(v(\omega_l))$, and therefore a different value of $\omega_B(\omega_l) = \omega_B(v(\omega_l))$. With adequate precision in the measurement of $\omega_B(\omega_l)$, it is possible to detect the deviation caused by the QG effect. The possibility of detecting the QG signature depends on the value of α_0 , with larger values resulting in a larger QG effect. The proposed experiment would then result

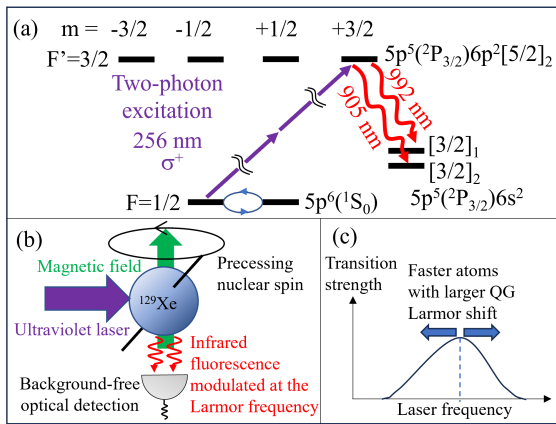


FIG. 1. (a) The partial energy level diagram of ^{129}Xe . A circularly-polarized ultraviolet laser drives spin-selective two-photon excitation in hyperpolarized ^{129}Xe atoms, where the excited state emits infrared light via radiative decay. The nuclear spin of the atoms precesses around an applied magnetic field, which is perpendicular to the laser propagation direction. Correspondingly, the ground state population coherently oscillates between the two magnetic sublevels, resulting in oscillation of the emitted infrared fluorescence. The latter is detected for extraction of the precession (Larmor) frequency. (b) Illustration of the proposed experiment. (c) Tuning the laser to different frequencies in the Doppler-broadened profile of the two-photon transition corresponds to different atom velocities, which in turn are associated with different QG shifts of the Larmor frequency.

either in a measurement of α_0 or provide an upper bound for its value. It should be noted that while not all atoms that are probed at a specific ω_l have the same velocity. Rather, they have the same longitudinal velocity. Due to the symmetry of the Maxwell-Boltzmann distribution, the contribution of the transverse velocity components is the same for any excitation frequency. Therefore, here they are ignored, since we are only aiming to resolve the difference between Larmor frequencies at different laser excitation frequencies.

We note that optical magnetometry is advantageous since the measurement is performed *in situ* and not at a distance as with other high-precision magnetometers, e.g., superconducting quantum interference devices (SQUIDs) [17]. Also, SQUIDs need to be cryogenically cooled, introducing significant technical challenges, while here we propose a method with room temperature operation. The main advantages of using hyperpolarized ^{129}Xe are the two-photon electronic transitions at frequencies that are low relative to other noble gases, and very long coherence time of its nuclear spin (scale of hours) at room temperature [18, 19], characteristic of noble gas isotopes with a nuclear spin of 1/2. The latter stems from the fact that the only non-zero angular momentum of the ground state of ^{129}Xe is the nuclear spin of 1/2, as the full electronic shell configuration has net zero electronic spin and orbital angular momenta. In hyperpolarized ^{129}Xe , the electrons have been pumped to a single magnetic sub-

level of the ground state, which means that the ^{129}Xe atoms are nuclear spin-polarized, and their nuclear spins can coherently precess under the influence of an external magnetic field with very little perturbation by the external environment. Another attractive feature of the proposed scheme is the use of a UV-excited state that decays via NIR emission, which provides a background-free signal that is easy to detect with technologically mature low-noise detectors.

The figure of merit used in this paper is the fractional sensitivity S , defined as $S = \delta\omega_B/\omega_B$, where $\delta\omega_B$ is the statistical uncertainty in the detected Larmor frequency ω_B . To detect the expected shift in the Larmor frequency due to QG, the Larmor frequency must be measured at minimum at two laser frequencies (preferably more), $\omega_{l,1}$ and $\omega_{l,2}$, with a fractional sensitivity that satisfies $S \leq |\omega_B(\omega_{l,1}) - \omega_B(\omega_{l,2})|/\omega_B(\omega_{Xe}) = |\mathcal{C}(\omega_{l,1}) - \mathcal{C}(\omega_{l,2})|$. If one measurement is taken on resonance ($\omega_l = \omega_{Xe}$) and the other at a frequency corresponding to velocity v , then to detect the QG signature we need $S \leq \mathcal{C}(\omega_l)$. With this figure of merit we can determine the minimum detectable value of α_0 , denoted $\alpha_{0,\min}$. Then the minimum possible detectable α_0 is given by $\alpha_{0,\min} = S \cdot (M_p c/mv)$ where both S and v depend on the laser frequency. We show in Section IV that, e.g., a fractional sensitivity on the order of 10^{-14} is required for detecting $\alpha_0 \approx 10^9$.

The proposed experimental setup consists of a small, spherical cell that contains xenon gas. The cell is contained within an apparatus that generates an extremely uniform magnetic field, and is illuminated by a DUV laser. The fluorescence emitted by the excited xenon atoms is collected into an optical detector. More details and feasibility estimation of required experimental conditions are discussed in Section III. The essence of the experimental procedure is as follows:

1. Prepare the xenon atoms in a spin-polarized state, e.g., via spin-exchange optical pumping [20].
2. Place the atoms in a magnetic field and illuminate them with circularly polarized laser light that propagates perpendicularly to the magnetic field direction, and has a frequency near a resonance of a two-photon transition in xenon.
3. As the atoms precess in the magnetic field, get excited by the laser and decay back to the ground state, measure their infrared emission, which oscillates at the Larmor frequency.
4. Repeat steps 1-3 until the fractional sensitivity has reached the desired level through statistical averaging.
5. Repeat steps 1-4 for different laser frequencies within the Doppler broadened lineshape of the two-photon transition.

In the following two sections we outline the fluorescence detection model and derive an analytical expression for

the fractional sensitivity as a function of experimental parameters.

B. Detected Signal Model

Towards determining the fractional sensitivity, we develop an analytical model for the infrared photon detection rate. We begin by determining the rate at which the xenon atoms absorb the DUV laser light. The two-photon absorption rate per atom is [21]

$$W^{(2)}(\omega_l) = \hat{\sigma}^{(2)}(\omega_l) \left(\frac{I}{\hbar\omega_l} \right)^2, \quad (5)$$

where $\hat{\sigma}^{(2)}(\omega_l)$ is the two photon cross-section, I is the intensity of the laser, ω_l is the angular frequency of the laser radiation, and \hbar is the reduced Planck's constant.

We express the Doppler-broadened two-photon cross-section with experimentally determined parameters as (see Appendix A)

$$\hat{\sigma}^{(2)}(\omega_l) = \alpha_{\text{Xe}} (\hbar\omega_l)^2 \sqrt{\frac{\ln 2}{\pi}} \frac{2}{\Delta\omega_D} \times \exp \left[-\ln 2 \left(\frac{2}{\Delta\omega_D} \right)^2 (\omega_l - \omega_{\text{Xe}})^2 \right], \quad (6)$$

where α_{Xe} is the two-photon absorption coefficient and the full-width at half-maximum (FWHM) of the Doppler broadened absorption profile is [13]

$$\Delta\omega_D = \frac{\omega_{\text{Xe}}}{c} \sqrt{\frac{8k_B T_{\text{Xe}} \ln 2}{m_{\text{Xe}}}}, \quad (7)$$

where T_{Xe} is the temperature of the atomic gas, k_B is the Boltzmann constant, m_{Xe} is the mass of a ^{129}Xe atom, c is the speed of light, and ω_{Xe} is the transition resonance angular frequency in the atom's frame of reference. The two-photon transition rate per atom is therefore

$$W^{(2)}(\omega_l) = \alpha_{\text{Xe}} \sqrt{\frac{\ln 2}{\pi}} \frac{2}{\Delta\omega_D} \left(\frac{2P_l}{\pi w_0^2} \right)^2 \times \exp \left[-4 \ln 2 \left(\frac{\omega_l - \omega_{\text{Xe}}}{\Delta\omega_D} \right)^2 \right], \quad (8)$$

where $P_l = I\pi w_0^2/2$ is the laser power, and w_0 is the beam radius at $1/e^2$ of maximum intensity, where we assume a Gaussian beam with peak intensity I .

By design of the experimental geometry, the beam size is approximately constant throughout the interaction region, i.e., $b = 2z_R \gg L$, where $z_R = \pi w_0^2/\lambda$ is the Rayleigh range, b is the beam's confocal parameter, and L is the interaction length. Therefore, the interaction volume is $L\pi w_0^2$, and the ensemble absorption rate is $W^{(2)}(L\pi w_0^2) n_{\text{Xe}}$, where n_{Xe} is the number density of ^{129}Xe atoms in the gas. We note that n_{Xe} is related to the temperature T_{Xe} and pressure p_{Xe} of the gas through

ideal gas law, $n_{\text{Xe}} = \eta_{^{129}\text{Xe}} p_{\text{Xe}} / (k_B T_{\text{Xe}})$, where $\eta_{^{129}\text{Xe}}$ is the isotopic fraction of ^{129}Xe in the xenon gas. Every atom that undergoes two-photon excitation will eventually emit an infrared photon, where a fraction ϵ_T of these photons will be detected, therefore the mean rate of infrared photon detection is

$$\bar{n}_f = \frac{1}{2} W^{(2)} n_{\text{Xe}} (L\pi w_0^2) \epsilon_T, \quad (9)$$

where ϵ_T is the detection efficiency of the emitted infrared photons, and the factor of $\frac{1}{2}$ accounts for the fact that in an unpolarized atomic ensemble only half of the atoms get excited (i.e., half of the ground-state atoms are in the $m = -1/2$ magnetic sublevel while the other half are in the $m = +1/2$ sublevel). When the atomic ensemble is polarized and subjected to an external magnetic field, the infrared photon detection rate becomes

$$n_f(t) = \bar{n}_f \left[1 + P_{\text{Xe}} \cos(\omega_B t) e^{-t/T_d} \right], \quad (10)$$

where T_d is the spin polarization's decay rate, $0 \leq P_{\text{Xe}} \leq 1$ is the initial degree of spin polarization.

C. Detection Noise and Sensitivity Model

The statistical uncertainty in the Larmor frequency detection arises due to noise that accompanies the photodetector signal. Therefore, the fractional sensitivity is $S = \sigma_{\omega_B} / \omega_B$, where $\sigma_{\omega_B}^2$ is the total noise variance in the measured Larmor frequency. The sensitivity is ultimately limited by two fundamental sources of noise: shot noise and projection noise [22]. Shot noise results from the discrete statistical nature of photons, described by Poisson statistics, with variance $\sigma_{\omega_B,SN}^2$. Projection noise is a result of the Heisenberg uncertainty principle, and we label its variance $\sigma_{\omega_B,PN}^2$. The total noise variance is $\sigma_{\omega_B}^2 = \sigma_{\omega_B,SN}^2 + \sigma_{\omega_B,PN}^2$. The statistical uncertainty is reduced by averaging the results of N_m measurements of ω_B (step 4 in Section II A), thus the fractional sensitivity is given by

$$S = \sqrt{\frac{\sigma_{\omega_B}^2}{N_m \omega_B^2}} = \frac{1}{\sqrt{N_m} \omega_B} \sqrt{\sigma_{\omega_B,SN}^2 + \sigma_{\omega_B,PN}^2}. \quad (11)$$

The detected signal of Eq. 10 is a sum of a DC component and a decaying sinusoidal, where we are interested in extracting the sinusoidal's oscillation frequency, ω_B . The variance in the extracted frequency due to shot-noise is (see Appendix B)

$$\sigma_{\omega_B,SN}^2 = \frac{12T_d \left(\sqrt{1 + \frac{P_{\text{Xe}}^2}{2}} \right) (e^{2T_m/T_d} - 1)}{\bar{n}_f P_{\text{Xe}}^2 T_m^4}, \quad (12)$$

where T_m is the time duration of a single measurement (step 3 in Section II A).

The variance due to spin projection noise in a single measurement of the Larmor angular frequency is [22]

$$\sigma_{\omega_B, PN}^2 = \frac{(2\pi)^2}{T_d N_{Xe} T_m}, \quad (13)$$

where $N_{Xe} = (L\pi w_0^2) n_{Xe}$ is the number of xenon atoms in the interaction volume.

Eqs. 11 - 13 provide the ultimate fractional precision of the proposed experiment for a given set of experimental parameter values. This fractional sensitivity depends on several experimentally controlled parameters, including the magnetic field strength and uniformity that determine the Larmor frequency and spin polarization decay time; the interaction volume, initial polarization, isotopic fraction of ^{129}Xe , gas temperature, and gas pressure impact the decay time and the number of interacting atoms; duration of one measurement and number of measurements taken; and laser power, beam waist radius, and frequency. In the following two sections we detail the values of these parameters.

III. NATURAL AND CONSTRAINED PARAMETER VALUES

In this section we provide details on parameter values that we use in the calculation of the fractional sensitivity in the following section. We detail atomic properties of ^{129}Xe , macroscopic properties of xenon gas, characteristics of the magnetic field, laser configuration, and explain how all these interact to impact the proposed experimental measurement.

The electronic spectrum and physical properties of xenon isotopes are well known. The reported gyromagnetic ratio of ^{129}Xe is $\gamma = 2\pi \times 11.78 \times 10^6 \text{ Hz/T}$ [23–25]. The natural abundance of the isotope ^{129}Xe is 26% [20]. While isotopically enriched xenon gas with significantly more than 80% ^{129}Xe content is commercially available, here we conservatively assume $\eta_{^{129}\text{Xe}} = 0.8$. The $5p^6(^1S_0) \rightarrow 5p^5(^2P_{3/2})6p^2[5/2]_2$ two-photon transition is resonantly driven with photons at a DUV wavelength of 256.017 04(1) nm [26]. An excited xenon atom will decay through one of two channels: $5p^5(^2P_{3/2})6p^2[5/2]_2 \rightarrow 5p^5(^2P_{3/2})6s^2[3/2]_1$ with a wavelength of 992.3 nm [26] and a splitting ratio of 0.637 [27], or $5p^5(^2P_{3/2})6p^2[5/2]_2 \rightarrow 5p^5(^2P_{3/2})6s^2[3/2]_2$ with a wavelength of 904.5 nm [26] and a splitting ratio of 0.363 [27] (see Fig. 1). By using circularly polarized light, we can selectively excite only the $m = -1/2$ magnetic sublevel of the ground state, so that population oscillation between the two ground state magnetic sublevels is apparent in the detected infrared fluorescence. Therefore, care must be taken to avoid also driving the transition from the ground state $m = +1/2$ magnetic sublevel to the $m = +5/2$ magnetic sublevel of the $F' = 5/2$ state in the $5p^5(^2P_{3/2})6p^2[5/2]_2$ hyperfine manifold. The hyperfine splitting between the

$F' = 5/2$ and $F' = 3/2$ state is $\Delta\omega_{hfs} = 2\pi \times 3.4105 \text{ GHz}$ [28]. Below we show that the Doppler broadened absorption profile FWHM is $\Delta\omega_D = 2\pi \times 1.26 \text{ GHz}$, so $\Delta\omega_D < \Delta\omega_{hfs}$, meaning we can selectively excite the transition to the $F' = 3/2$ state while avoiding excitation of the $F' = 5/2$ state with a proper choice of laser parameters, as follows. We define the laser cut-off frequency, $\omega_{l, \text{cut-off}}$, as the laser frequency where the two-photon cross section of the $F' = 5/2$ state is 10 time lower than the $F' = 3/2$ two-photon cross section, i.e., $\hat{\sigma}_{F=5/2}(\omega_{l, \text{cut-off}})/\hat{\sigma}_{F=3/2}(\omega_{l, \text{cut-off}}) = 0.1$. Using Eq. 6, this yields $\omega_{\text{cut-off}} = \omega_{Xe} - 1.18\Delta\omega_D$. For all higher frequencies, this ratio is lower. Below we show that $\omega_{\text{cut-off}}$ is outside the region of interest for practical experiments, since the $F' = 3/2$ two-photon cross section is too low so far off resonance. In fact, in the region of interest $\hat{\sigma}_{F=5/2}/\hat{\sigma}_{F=3/2} \sim 10^{-2}$. Therefore, for all excitation frequencies of interest, the transition to the $F' = 5/2$ state is neglected. Finally, there are multiple reported values of the two-photon absorption coefficient, α_{Xe} [29, 30]. Here we use the most recently reported value of $83(25) \text{ cm}^4/\text{J}^2$ [30].

The Doppler FWHM is determined by natural properties of xenon (mass and resonance frequency) and an experimentally controlled parameter, i.e., gas temperature, with higher temperature resulting in a wider Doppler width. For simplicity of the experimental apparatus and procedure, we assume the gas is at room temperature, $T_{Xe} = 293.15 \text{ K}$, which results in a Doppler FWHM of $\Delta\omega_D = 2\pi \times 1.26 \text{ GHz}$. We note that precise control of this temperature is not required, since precision of a few degrees K (commonly achieved with ordinary room temperature control) would only change the excitation rate by tiny fraction, and would not impact the measured Larmor frequency and QG correction, which depend only on the applied magnetic field strength and laser frequency.

Under the experimental conditions proposed here, Doppler broadening dominates over all other broadening mechanisms. The natural linewidth of the two-photon transition is about 4.3 MHz [27]. Collisional broadening has been measured to be 18.6 MHz/mbar [29]. Therefore, in order to keep collisional broadening insignificant compared to Doppler broadening, we need to keep the pressure much lower than 66 mbar. Here we consider a pressure of 10 mbar, corresponding to collisional broadening of 186 MHz. Transit-time broadening width is given by $\sim 0.4v/w_0$ [13]. At room temperature, the most probable speed of a Boltzmann-Mawell distribution is $\sqrt{2k_B T/m_{Xe}} \approx 200 \text{ m/s}$, where m_{Xe} is the mass of ^{129}Xe . Therefore, in order to keep Doppler broadening dominant over transit-time broadening, we require $w_0 \gg 0.4 \cdot 2\pi v/\Delta\omega_D \approx 63 \text{ nm}$. Even when considering speeds 10 times higher than the most probable speed, we only need to keep the beam radius much greater than $0.63 \mu\text{m}$, which is very easy to satisfy. As detailed below, we propose using beam radii of at least $100 \mu\text{m}$, corresponding to a maximum transit-time broadening of 8 MHz at 10 times the most probable velocity. Compared

to the Doppler width of 1.26 GHz, all of these broadening mechanisms make a negligible contribution of about 200 MHz at most. Therefore, we neglect them and consider only Doppler broadening.

The initial degree of ensemble spin polarization and its decay rate have a strong impact on the sensitivity of the proposed measurement. Methods for spin-polarizing ^{129}Xe are well established [20] and will not be detailed here. We estimate the initial spin polarization, P_{Xe} , based on published values in a systematic study of spin exchange optical pumping of ^{129}Xe , where a polarization fraction of 90% has been experimentally achieved for gas pressure of 400 mbar [20]. While even higher polarization is likely possible at the lower pressure considered here, we conservatively assume $P_{\text{Xe}} = 0.9$ for gas pressure of 10 mbar. Spin polarization can decay via depolarization or through dephasing. Depolarization is also called longitudinal decay, with a characteristic decay time T_1 , and dephasing is commonly termed transverse decay, with a characteristic timescale T_2 . Overall, spin polarization relaxation is dominated by T_2 , since any effect that reduces T_1 also reduces T_2 . The spatial uniformity of the magnetic field is critical in achieving long transverse spin relaxation times. If different atoms experience a different magnetic field, or equivalently the same atoms experience a varying magnetic field as they perform diffusive motion in the gas container, then their spin precession frequency will vary and they will become out of phase with each other. Correspondingly, the transverse relaxation time will decrease according to $T_2 = 2\pi/\gamma\Delta B$, where ΔB is the spatial variation in the magnetic field across the gas volume. However, the nature of the diffusive motion of the atoms will change this dephasing rate, and may lead to a different value of T_2 , depending on gas pressure [18]. A recent experiment recorded T_1 and a T_2 values up to 99 hours and 8000 s, respectively, under a magnetic field variation of 240 pT across a spherical container with 2 cm diameter holding a 4:1 xenon:nitrogen gas mix with xenon partial pressure of about 50 mbar, where lower pressure correlated with longer T_2 [18]. For these conditions, $2\pi/\gamma\Delta B \approx 353$ s, which is much smaller than the experimentally measured value. The difference is attributed to the atoms' limited diffusive motion slowing down the rate of dephasing. In another experiment, a field variance of $\Delta B = 800$ fT over a distance of 2 cm in a nominal magnetic field strength of $B = 2.7$ μT was demonstrated [31]. We note that we obtained this value by using graph extraction software to find the minimum field variation across 2 cm in the published graph of ΔB vs. spatial position. However, this might be misleading, since this value is below the experimental measurement precision, which is better than $\Delta B_L = 3$ pT/cm. Therefore, we conservatively assume a field variation of $\Delta B = 6$ pT over a sphere with 2 cm diameter. This corresponds to a transverse relaxation time of $T_2 = 2\pi/\gamma\Delta B = 3.93$ hours, where we did not account for any diffusive effects that may increase T_2 further. The Larmor frequency corresponding to a

2.7 μT magnetic field is $2\pi \times 31.8$ Hz. We note that the coil system used to produce this field provides plenty of room and clearance (more than 50 cm on each side) for the gas container, with optical access on six sides that can accommodate the excitation laser beam and fluorescence collection optics for the detection system in the experiment proposed here.

The power of the two-photon excitation laser has a strong impact on the fractional sensitivity. As noted above, the excitation wavelength of 256 nm is in the DUV, where achieving high laser power and frequency stability are technically challenging. The established approach for addressing this challenge is through frequency upconversion via cascaded nonlinear wave mixing of near-infrared lasers, either CW or ultrafast frequency combs. Since the efficiency of nonlinear wave mixing strongly scales with intensity, single-pass upconversion of CW lasers suffers from low efficiency, producing very limited DUV power. Instead, researchers perform the upconversion process inside a cavity, where very high optical power is built up and the laser light effectively passes through the nonlinear medium many times [32]. For example, Burkley et al. have generated 1.4 W at 243.1 nm with a linewidth < 10 kHz using a 10 W infrared seed laser [33]. Another upconversion method uses frequency combs, which are frequency-stabilized pulsed lasers. Frequency combs usually operate with MHz-GHz pulse repetition rate, where pulse-to-pulse coherence leads to a set of very narrow spectral features ("comb teeth"), equally spaced at intervals equal to the pulse repetition rate [34]. Their short pulse duration (on the femtosecond-picosecond scale) leads to very high intensity and efficient single-pass frequency conversion. For example, Yang et al. [35] demonstrated a DUV frequency comb at 258 nm that boasts a sub-Hz linewidth and delivers 1.58 W of power, produced from a 41 W infrared frequency comb seed laser. More recently, phase-stabilized femtosecond lasers with wavelength near 1 μm have reached 1 kW power [36], and a similar system yielded 10.4 kW power [37]. At the same time, frequency conversion from such high-power sources has also been advancing: Rothhardt et al. have demonstrated a femtosecond laser delivering 100 W at 343 nm from a 620 W infrared seed laser [38]. Therefore, here we consider a DUV laser power range of 1 W to 100 W, where the laser can be tuned across the Doppler lineshape, and the laser linewidth is $\ll \Delta\omega_D$. These laser properties have either been demonstrated or have strong evidence for their feasibility with existing or near-future technology.

An additional constraint must be considered when a frequency comb laser is considered for the proposed experiment. When a frequency comb excites a two-photon transition, comb teeth that are equally spaced around the resonance frequency combine coherently to drive the transition, resulting in a transition rate equivalent to a CW laser of the same average power [39, 40]. However, here we are proposing to use a comb to selectively excite a subset of atoms, with a particular velocity, out of

a large number of atoms with a wide velocity distribution, while also avoiding the transition to the $F' = 5/2$ state. In other words, we wish to excite only a narrow spectral span out of the Doppler broadened spectrum of the transition to the $F' = 3/2$ state. If the comb's pulse repetition rate (equal to its spectral "teeth" spacing) is smaller than the Doppler width, then sets of comb teeth will combine to excite different velocity subsets of atoms. Also, if the pulse repetition rate is close to the hyperfine splitting (i.e., no more than a Doppler width away), then the transitions to both the $F' = 3/2$ and $F' = 5/2$ states get excited. Therefore, in order to be able to excite a single velocity group to the $F' = 3/2$ state alone, the comb's repetition rate must significantly exceed the combined hyperfine splitting and Doppler width. We consider a pulse repetition rate, f_{rep} , that is triple the Doppler FWHM plus the hyperfine splitting to be sufficient, i.e., $2\pi f_{\text{rep}} \geq 3\Delta\omega_D + \Delta\omega_{hf_s}$. Under this condition, even in the extreme case where the comb is tuned off the $F' = 3/2$ resonance by a full FWHM, to $\omega_{Xe} + \Delta\omega_D$, the next nearest resonance is in the $F' = 5/2$ level, where the excitation's cross section is 2.5×10^{-4} times smaller, and therefore can be neglected. For the case considered here, our condition translates into a pulse repetition rate of at least 7.2 GHz, which is commonly achieved in various near-infrared comb systems [41, 42]. We note that increasing the pulse repetition rate reduces pulse energy for the same average power, however it makes ultrafast pulse amplification to high power more straight-forward since pulse-distorting parasitic nonlinear effects are better mitigated [43–45]. Overall, the lower pulse energy and shorter pulse duration roughly balance out, delivering similar peak intensity, and therefore similar nonlinear upconversion efficiency downstream. Additionally, the repetition rate of a comb can be increased from the MHz to the GHz range using an external Fabry-Perot cavity with high transmission [46–49]. Therefore, the required pulse repetition rate is well within reach of existing technology.

Finally, the fractional sensitivity depends on the detection efficiency of the emitted infrared photons, $\epsilon_T = \epsilon_{\text{det}}\epsilon_{\text{geo}}$, where ϵ_{det} is the efficiency of the detector and ϵ_{geo} is the fraction of fluorescence photons that are collected into the detector. As noted above, the emission is in the wavelengths of 992 nm and 905 nm. These are in the near-infrared and therefore can be detected with a high efficiency, e.g., using an avalanche photodetector. ϵ_{geo} depends on the collection optics geometry, whose details are out of the scope of the present work. Standard methods commonly achieve $\sim 50\%$ collection efficiency and $\sim 45\%$ detection efficiency, for an overall efficiency of $\sim 22.5\%$ [50]. Here we conservatively assume an overall efficiency of $\epsilon_T = 0.1$, which incorporates the efficiency of both the detector and the photon collection geometry.

A summary of all parameter values are shown in Table I. The values that are calculated from these parameters are shown in Table II, some of which were obtained via

the optimization procedure detailed in Section IV.

IV. SENSITIVITY OPTIMIZATION, DETECTION BOUNDS AND DISCUSSION

A. Optimizable Parameter Values

With the experimental parameter values detailed in the previous section there are still five values that have not been given a specified value: w_0 , T_m , N_m , ω_l , and P_l . We treat these in this section.

The interaction between the xenon atoms, the magnetic field, and the laser light occurs in a volume defined by the interaction length, L , and the beam waist diameter, w_0 . We have assumed that the interaction length is much shorter than the beam's confocal parameter and therefore we take the beam diameter to be constant along L . In the calculations carried out below, the beam waist radius is optimized for each value of laser power by setting it to the value that minimizes the fractional sensitivity of Eq. 11, as derived in Appendix C. When the laser is on resonance with the two-photon transition and with laser power values ranging from 1 W to 100 W, the optimal beam radii range from 100 μm to 999 μm , with corresponding confocal parameter of 24 cm to 24 m, which satisfies our requirement that $b \gg L = 2$ cm.

The power of the laser, P_l , and the number of measurement iterations, N_m , will unambiguously give a more precise result as they increase. As explained in the preceding section, we constrain the laser power to feasible values of 1-100 W. Below, we keep N_m bounded by a total experimental measurement time of 1 year, in order to keep the proposed experiment within the bounds of feasibility. The remaining two variables are the duration of a single experiment, T_m , and the laser angular frequency, ω_l . Next, we optimize them to numerically yield minimal values of the fractional sensitivity of Eq. 11.

The goal of optimizing the value of T_m is to find the duration of a single measurement that delivers a given sensitivity with the minimal duration of an entire set of measurements, $N_m T_m$. To find this optimal value we calculated S with different P_l and ω_l while sweeping over a range of values for T_m and finding the number of experiments required to achieve a specific value of S . For all considered values of P_l and ω_l , which were 1-100 W and $\omega_{Xe} - 1.75\Delta\omega_D$ to $\omega_{Xe} + 1.75\Delta\omega_D$, respectively, the optimal value which minimizes $T_m N_m$ was found to be $T_m = 1.19T_d$ in all cases. This value of T_m was used in all the calculations below.

In optimizing ω_l we considered the case where one measurement is taken on two-photon resonance and another measurement is taken at a laser frequency that minimizes the value of α_0 that can be detected for given values of P_l and N_m , i.e., we find the minimum value of $\alpha_{0,\text{min}} = S(\omega_l, P_l, N_m)(M_p c/mv)$ for this set of P_l and N_m values. There are two opposing factors influencing the value of $\alpha_{0,\text{min}}$ as ω_l is varied. The first factor is the

TABLE I. Parameter values estimated from published literature.

Name	Symbol	Value	Ref
Laser Power limits	P_l	1 W to 100 W	See Section III
Two-photon transition resonant wavelength	λ_{Xe}	256.017 04(1) nm	[26]
Two-photon transition resonant angular frequency	ω_{Xe}	$7.357\,524\,2(3) \times 10^{15}$ 1/s	[26]
^{129}Xe nuclear spin gyromagnetic ratio	γ	$2\pi \times 11.78 \times 10^6$ Hz/T	[23–25]
Two-photon transition absorption coefficient	α_{Xe}	$83 \text{ cm}^4/\text{J}^2$	[29]
Magnetic field	B	$2.7 \mu\text{T}$	[31]
Variation in the magnetic field	ΔB	6 pT	[31]
Xenon gas temperature	T_{Xe}	300 K	[18]
Xenon gas pressure	p_{Xe}	10 mbar	[18, 20]
Isotopic fraction of ^{129}Xe	$\eta_{^{129}\text{Xe}}$	80 %	[20]
Initial spin polarization	P_{Xe}	90 %	[20]
Interaction length	L	2 cm	[18, 20]
Total efficiency of fluorescence detection	ϵ_T	10 %	[50]

TABLE II. Values calculated from parameters from Table I.

Name	Symbol	Value
Larmor frequency without QG	ω_B	$2\pi \times 31.78$ Hz
Laser beam radius	w_0	100 μm to 999 μm
Spin relaxation time	T_d	3.93 hours
Doppler profile FWHM	$\Delta\omega_D$	$2\pi \times 1.27$ GHz
Duration of a single measurement	T_m	4.67 hours
Optimal laser frequency	$\omega_{l,opt}$	$7.357\,537\,8 \times 10^{15}$ 1/s

decreased velocity of the atoms that are being probed as ω_l approaches ω_{Xe} , meaning a smaller v and therefore higher $\alpha_{0,min}$. The second factor is the increased Doppler-broadened two-photon cross-section as ω_l approaches ω_{Xe} , resulting in a higher two-photon transition rate and therefore smaller S and lower $\alpha_{0,min}$. These opposing trends produce a minimum in $\alpha_{0,min}$, which we find numerically, where S is given by Eq. 11 and v is given by Eq. 4. For all values of P_l and N_m that we checked, the minimum was always at $\omega_{l,opt} = \omega_{Xe} + 0.85\Delta\omega_D$. A few examples are shown in Fig. 2. Note that the curvature of the curves in Fig. 2 is small, meaning that deviating from the optimal frequency does not greatly increase the value of $\alpha_{0,min}$. For example, using $\omega_l = \omega_{Xe} + 0.5\Delta\omega_D$ would increase $\alpha_{0,min}$ by no more than 30%. This implies that adding more measurement points at different laser frequencies would not change the order of magnitude of the duration of the experiment, and therefore is still feasible.

B. Calculation Results

The calculation results are shown in Fig. 3 as three superimposed contours as a function of laser power and the total measurement time for a single laser frequency, $T_m N_m$. For convenience the plot includes horizontal lines that mark total times of one day, one week, and one month. The three overlaid contours depict $\alpha_{0,min}$ for $\omega_l = \omega_{l,opt}$, the corresponding optimized fractional

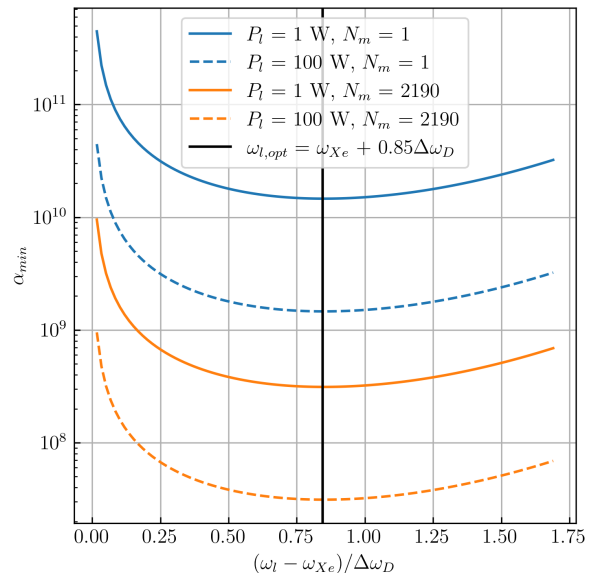


FIG. 2. Minimum detectable QG correction coefficient, $\alpha_{0,min}$, as a function of laser frequency, ω_l , for different values of laser power, P_l , and number of measurements, N_m . Four examples are shown with a combination of two values for (1 W and 100 W) and two values for N_m (1 and 2190). The latter correspond total measurement times, $N_m T_m$, of 4.7 hours and 1 year, respectively. The optimal laser frequency, $\omega_{l,opt} = \omega_{Xe} + 0.85\Delta\omega_D$, is identified by a black vertical line.

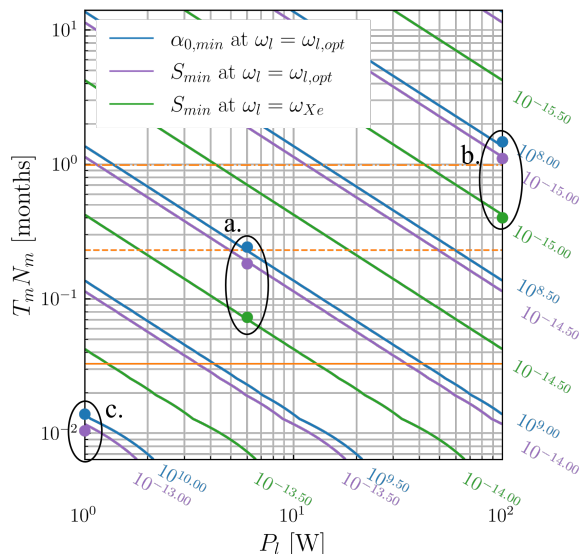


FIG. 3. The minimum values of the QG correction coefficient $\alpha_{0,min}$ at the optimal laser frequency $\omega_{l,opt}$ (blue), the corresponding optimized fractional sensitivity S_{min} at $\omega_l = \omega_{l,opt}$ (purple), and the optimized fractional sensitivity on two-photon resonance, S_{min} at $\omega_l = \omega_{Xe}$ (green). Notable time scales of 1 day (solid), week (dashed), and month (dot-dashed) are indicated in orange.

sensitivity, S_{min} , and the value of S_{min} for $\omega_l = \omega_{Xe}$.

Fig. 3 is an aid to determine the feasibility of detecting a given value of the QG correction coefficient, α_0 , for a given laser power, by establishing the duration of the required measurement. This is done in three steps. First, determine the total measurement time, $T_m N_m$, to detect the specified value of α_0 with the available laser power and with the laser frequency tuned to its optimal value, i.e., $\omega_l = \omega_{l,opt}$. Next, determine the corresponding optimized fractional sensitivity, S_{min} at $\omega_l = \omega_{l,opt}$. Finally, determine the total measurement time to achieve the same fractional sensitivity when the laser is tuned to the two-photon resonance, i.e., $\omega_l = \omega_{Xe}$.

We next provide a few examples that illustrate the feasibility of measuring various values of α_0 . The first example is indicated in Fig. 3 by the three markers in the ellipse marked “a”, which lie along the vertical line corresponding to a laser power of $P_l = 6$ W. The blue marker indicate the a target value of $\alpha_0 \approx 10^9$, where the required time to measure the Larmor frequency with adequate precision using a laser frequency of $\omega_l = \omega_{l,opt}$ is approximately 1 week. This corresponds to a fractional sensitivity of $S \approx 10^{-14}$ (purple marker). To achieve the same fractional sensitivity at resonance, i.e., with a laser frequency $\omega_l = \omega_{Xe}$, a total time of $T_m N_m \approx 2$ days is required (green marker). This means that the whole experiment will take about 1.5 weeks, which is feasible. Taking additional data points at other laser frequencies is also feasible, since each would take ~ 9 days of mea-

surement (see discussion of Fig. 2). This example shows that detecting $\alpha_0 \approx 10^9$ is feasible with just a minor improvement to existing laser technology.

As another example, indicated by the markers in the ellipse marked “b” in Fig. 3, consider an experiment using a laser with $P_l = 100$ W and a target of $\alpha_0 \approx 10^8$. With a laser frequency $\omega_l = \omega_{l,opt}$ this requires a measurement time of ~ 6 weeks, where the corresponding sensitivity is $S \approx 10^{-15}$. To achieve this sensitivity on resonance would take ~ 2 weeks, for a total measurement time of 2 months, where each additional laser frequency data point needs ~ 8 weeks to complete. While this is still feasible, such an experiment would be a very challenging task, even for the extrapolated DUV laser power of $P_l = 100$ W that we expect to be available in the near future.

For a final example, consider an experiment using a laser with $P_l = 1$ W and a target of $\alpha \approx 10^{10}$, corresponding to the markers in the ellipse marked “c” in Fig. 3. The measurement with a laser frequency $\omega_l = \omega_{l,opt}$ will take about 12 hours and have a sensitivity of $S \approx 10^{-13}$. For on-resonance measurement, this would take about 3 hours (less than a single optimized measurement time T_m). This gives a total measurement time of about 15 hours for two data points, with additional points taking only ~ 16 hours each. This example shows that detecting $\alpha_0 \approx 10^{10}$ is within reach of existing technology.

V. CONCLUSION

In conclusion, we proposed using two-photon spectroscopy of a thermal ensemble of hyperpolarized ^{129}Xe atoms to measure theoretically predicted QG-induced Larmor frequency variation. We quantitatively demonstrated the feasibility of this approach, where existing or near-future technology would provide sufficient precision to go beyond known bounds. Key technical aspects are a magnetic field with a high degree of spatial uniformity that leads to long coherence time of ^{129}Xe nuclear spin precession, and a high power DUV laser that can drive a two-photon transition at a high rate. Particularly, we modeled the detected signal and detection noise, culminating in an analytical expression that describes the fractional sensitivity in terms of the experimental parameters. We optimized the experimental parameters to detect the QG correction that is linear in momentum, parametrized by a coefficient α_0 , which existing experimental evidence bound be less than 10^{17} . Finally, we discuss the feasibility of detecting various values of α_0 , showing that 10^{10} is within reach of current technology, while 10^8 would be feasible with near-future laser capabilities, corresponding to improving the current bound by 7 and 9 orders of magnitude, respectively.

ACKNOWLEDGMENTS

We would like to thank Dr. Lindsay LeBlanc for helpful discussions and her support as a co-supervisor of James Maldaner. We acknowledge the support of the Natural Sciences and Engineering Research Council of Canada (NSERC), [funding reference number RGPIN-2019-05017]. We acknowledge the support of the Government of Canada's New Frontiers in Research Fund (NFRF), [NFRFE-2018-01220]. We acknowledge the support of Alberta Innovates [570922-21 and 212200789]. We acknowledge the support of Alberta's Quantum Technologies Major Innovation Fund [RCP-19-004-MIF]. We acknowledge the support of Quantum City [1059845-10].

Appendix A: Two-photon cross-section

Here we develop an analytical expression for the two-photon cross section, and make connections to parameters whose values are reported in literature. The two-photon cross-section is the product of three values: a photon statistics factor of the light source, $G^{(2)}$, the line-shape of the two-photon transition, $g(\omega)$, and the two-photon cross-section's value at line center, $\sigma_0^{(2)}$,

$$\hat{\sigma}^{(2)}(\omega) = \sigma_0^{(2)} g(\omega) G^{(2)}, \quad (\text{A1})$$

where ω is the angular frequency of the radiation.

We take $G^{(2)} = 1$ for a classically coherent light source. Here, Doppler broadening dominates the lineshape so we take it to be a Gaussian that is defined by the Doppler FWHM $\Delta\omega_D$. Published reports of two-photon cross-section measurements commonly write the Gaussian lineshape using a width parameter, β ,

$$g(\omega) = \exp\left[-\beta(\omega - \omega_0)^2\right], \quad (\text{A2})$$

where $\beta = \ln 2 \left(\frac{2}{\Delta\omega_D}\right)^2$ and the cross section is maximized at ω_0 . Additionally, the reported value is usually the two-photon absorption coefficient, $\alpha = \sigma_{tot}/(\hbar\omega)^2$, where σ_{tot} is spectrally integrated two-photon cross-section given by

$$\sigma_{tot} = \int_{-\infty}^{\infty} \sigma_0^{(2)} g(\omega) d\omega = \sigma_0^{(2)} \sqrt{\frac{\pi}{\beta}}. \quad (\text{A3})$$

We found it most convenient to express the two-photon cross-section using α and $\Delta\omega_D$,

$$\hat{\sigma}^{(2)}(\omega) = \alpha (\hbar\omega)^2 \sqrt{\frac{\ln 2}{\pi}} \frac{2}{\Delta\omega_D} \exp\left[-\ln 2 \left(\frac{2}{\Delta\omega_D}\right)^2 (\omega - \omega_0)^2\right] G^{(2)}. \quad (\text{A4})$$

In the main text the incident radiation is denoted $\omega = \omega_l$ and the resonant frequency is $\omega_0 = \omega_{Xe}$.

Appendix B: Photon shot noise

The variance in the estimation of the frequency of an exponentially decaying sinusoidal signal, due to shot noise in the signal's amplitude, is [51]

$$\sigma_\omega^2 = \frac{6n^2 (e^{2\Gamma T_m} - 1)}{\Gamma A^2 T_m^4}, \quad (\text{B1})$$

where n is the RMS noise spectral density amplitude at the frequency of the sinusoid, Γ is the decay rate of the signal, A is the initial amplitude of the signal, and T_m is the duration of the time interval taken into account for estimating the frequency.

Here, the signal is the oscillating part of the photodetector photocurrent corresponding to the infrared photon detection rate of Eq. 10. The detected photocurrent is

$$\begin{aligned} i &= en_f = e\bar{n}_f \left[1 + P_{Xe} \cos(\omega_B t) e^{-t/T_d}\right] \\ &= i_{DC} + i_{AC} e^{-t/T_d}, \end{aligned} \quad (\text{B2})$$

where e is the electron charge, and $i_{DC} = e\bar{n}_f$ and $i_{AC} = e\bar{n}_f P_{Xe} \cos(\omega_B t)$ are its DC and non-decaying AC components, respectively. Therefore, T_m is the time duration of a single measurement, $\Gamma = 1/T_d$, and $A = \max(i_{AC}) = e\bar{n}_f P_{Xe}$. The RMS noise spectral density amplitude in $i_n = i_{DC} + i_{AC}$ due to shot noise collected in a bandwidth of B_n is $n = \sqrt{\sigma_{i_n}^2/B_n}$, where $\sigma_{i_n}^2 = 2ei_{n,RMS}B_n$ is the shot noise variance in a photocurrent with RMS value of $i_{n,RMS}$, integrated over a bandwidth B_n . Overall, $n = \sqrt{2ei_{n,RMS}}$, where

$$i_{n,RMS} = \sqrt{i_{DC,RMS}^2 + i_{AC,RMS}^2} = e\bar{n}_f \sqrt{1 + \frac{P_{Xe}^2}{2}}. \quad (\text{B3})$$

Substituting the expressions for Γ , A and n into Eq. B1, we obtain

$$\sigma_{\omega_B,SN}^2 = \frac{12T_d \left(\sqrt{1 + \frac{P_{Xe}^2}{2}}\right) (e^{2T_m/T_d} - 1)}{\bar{n}_f P_{Xe}^2 T_m^4} \quad (\text{B4})$$

for the shot noise variance in the estimation of the frequency of the detected photocurrent signal.

Appendix C: Optimization of the laser beam radius

Using the analytical model of Eq. 11, we want to determine the laser beam radius, w_0 , that minimizes the fractional sensitivity. We begin by finding an expression for w_0 that corresponds to $\partial S/\partial w_0 = 0$, as follows. First, we write S^2 in a manner that shows its dependence on w_0 ,

$$S^2 = \frac{1}{\omega_B^2 N_m} \left(A_{SN} w_0^2 + \frac{A_{PN}}{w_0^2} \right), \quad (\text{C1})$$

where we defined

$$A_{SN} = \frac{12T_2 \left(1 + \frac{P_x^2}{2}\right)^{1/2}}{\alpha \sqrt{\frac{\ln 2}{\pi}} \frac{2}{\Delta\omega_D} \left(\frac{2P_l}{\pi}\right)^2 \frac{1}{2} n_{Xe} L \epsilon_f \pi P_{Xe}^2 T_m^4} \frac{(e^{2T_m/T_2} - 1)}{\exp\left[-4 \ln 2 \left(\frac{\omega_l - \omega_0}{\Delta\omega_D}\right)^2\right]} \quad (C2)$$

and

$$A_{PN} = \frac{2\pi}{T_2 n_{Xe} L \pi T_m}. \quad (C3)$$

Next, we differentiate the equation

$$\omega_B^2 N_m S^2 = A_{SN} w_0^2 + A_{PN} \frac{1}{w_0^2} \quad (C4)$$

and obtain

$$\omega_B^2 N_m \left(2 \frac{\partial S}{\partial w_0} S\right) = A_{SN} 2w_0 - A_{PN} 2 \frac{1}{w_0^3}. \quad (C5)$$

Finally, we set $\frac{\partial S}{\partial w_0} = 0$ and solve for w_0 , which yields

$$w_0 = \left(\frac{A_{PN}}{A_{SN}}\right)^{1/4}. \quad (C6)$$

Differentiating Eq. C5 produces

$$2\omega_B^2 N_m \left[\frac{\partial^2 S}{\partial w_0^2} S + \left(\frac{\partial S}{\partial w_0}\right)^2\right] = 2A_{SN} + 6A_{PN} \frac{1}{w_0^4}, \quad (C7)$$

which we evaluate for $w_0 = \left(\frac{A_{PN}}{A_{SN}}\right)^{1/4}$ where $\frac{\partial S}{\partial w_0} = 0$, so

$$2\omega_B^2 N_m \left[\frac{\partial^2 S}{\partial w_0^2} S\right]_{w_0 = \left(\frac{A_{PN}}{A_{SN}}\right)^{1/4}} = 8A_{SN}. \quad (C8)$$

All variables in this equation are positive, therefore $\left[\frac{\partial^2 S}{\partial w_0^2} S\right]_{w_0 = \left(\frac{A_{PN}}{A_{SN}}\right)^{1/4}}$ is positive, and the extremum at $w_0 = \left(\frac{A_{PN}}{A_{SN}}\right)^{1/4}$ is a minimum. This expression for w_0 is used in all calculations in this paper.

-
- [1] Isham, C. Prima facie questions in quantum gravity. *Canonical Gravity: From Classical To Quantum: Proceedings Of The 117th WE Heraeus Seminar Held At Bad Honnef, Germany, 13–17 September 1993*. pp. 1-21 (2005)
- [2] Ali, A., Das, S. & Vagenas, E. Proposal for testing quantum gravity in the lab. *Physical Review D*. **84**, 044013 (2011)
- [3] Bosso, P. & Das, S. Generalized uncertainty principle and angular momentum. *Annals Of Physics*. **383** pp. 416-438 (2017)
- [4] Li, J. & Qiao, C. The generalized uncertainty principle. *Annalen Der Physik*. **533**, 2000335 (2021)
- [5] Ali, A., Das, S. & Vagenas, E. Discreteness of space from the generalized uncertainty principle. *Physics Letters B*. **678**, 497-499 (2009)
- [6] Das, S. & Vagenas, E. Universality of quantum gravity corrections. *Physical Review Letters*. **101**, 221301 (2008)
- [7] Majumder, B. The generalized uncertainty principle and the Friedmann equations. *Astrophysics And Space Science*. **336**, 331-335 (2011)
- [8] Ali, A. No existence of black holes at LHC due to minimal length in quantum gravity. *Journal Of High Energy Physics*. **2012**, 1-14 (2012)
- [9] Ghosh, S. Quantum gravity effects in geodesic motion and predictions of equivalence principle violation. *Classical And Quantum Gravity*. **31**, 025025 (2013)
- [10] Das, S., Fridman, M., Lambiase, G. & Vagenas, E. Baryon asymmetry from the generalized uncertainty principle. *Physics Letters B*. **824** pp. 136841 (2022)
- [11] Bushev, P., Bourhill, J., Goryachev, M., Kukharchyk, N., Ivanov, E., Galliou, S., Tobar, M. & Danilishin, S. Testing the generalized uncertainty principle with macroscopic mechanical oscillators and pendulums. *Physical Review D*. **100**, 066020 (2019)
- [12] Fridman, M., Maldaner, J., Porat, G. & Das, S. Test of Quantum Gravity in Optical Magnetometers. *Submitted*.
- [13] Demtröder, W. *Laser Spectroscopy: Basic Concepts and Instrumentation*. (Springer Berlin Heidelberg, 2002),
- [14] Altieri, E., Miller, E., Hayamizu, T., Jones, D., Madison, K. & Momose, T. High-resolution two-photon spectroscopy of a 5 p 5 6 p ← 5 p 6 transition of xenon. *Physical Review A*. **97**, 012507 (2018)
- [15] Budker, D. & Romalis, M. Optical magnetometry. *Nature Physics*. **3**, 227-234 (2007)
- [16] Hecht, E. *Optics*. (Pearson Education, Incorporated, 2017)
- [17] Stolz, R., Schiffler, M., Becken, M., Thiede, A., Schneider, M., Chubak, G., Marsden, P., Bergshjorth, A., Schaefer, M. & Terblanche, O. SQUIDS for magnetic and electromagnetic methods in mineral exploration. *Mineral Economics*. **35**, 467-494 (2022)
- [18] Kilian, W., Haller, A., Seifert, F., Grosenick, D. & Rinneberg, H. Free precession and transverse relaxation of hyperpolarized 129 Xe gas detected by SQUIDS in ultralow magnetic fields. *The European Physical Journal D*. **42** pp. 197-202 (2007)
- [19] Anger, B.C., Schrank, G., Schoeck, A., Butler, K.A., Solum, M.S., Pugmire, R.J., Saam, B. & Saam, B. Gas-phase spin relaxation of Xe 129. *Physical Review A*. **78**, 043406 (2008)
- [20] Nikolaou, P., Coffey, A., Walkup, L., Gust, B., Whiting, N., Newton, H., Barcus, S., Muradyan, I., Dabaghyan, M., Moroz, G. & Others Near-unity nuclear polarization with an open-source 129Xe hyperpolarizer for NMR and MRI. *Proceedings Of The National Academy Of Sciences*.

- 110**, 14150-14155 (2013)
- [21] Saxon, R. & Eichler, J. Theoretical calculation of two-photon absorption cross sections in atomic oxygen. *Physical Review A*. **34**, 199 (1986)
- [22] Budker, D. & Kimball, D. Optical Magnetometry. (Cambridge University Press, 2013)
- [23] Marshall, H., Stewart, N., Chan, H., Rao, M., Norquay, G. & Wild, J. In vivo methods and applications of xenon-129 magnetic resonance. *Progress In Nuclear Magnetic Resonance Spectroscopy*. **122** pp. 42-62 (2021)
- [24] Tiesinga, E., Mohr, P., Newell, D. & Taylor, B. CODATA recommended values of the fundamental physical constants: 2018. *Journal Of Physical And Chemical Reference Data*. **50** (2021)
- [25] Pfeffer, M. & Lutz, O. 129Xe gas NMR spectroscopy and imaging with a whole-body imager. *Journal Of Magnetic Resonance, Series A*. **108**, 106-109 (1994)
- [26] Saloman, E. Energy levels and observed spectral lines of xenon, Xe I through Xe LIV. *Journal Of Physical And Chemical Reference Data*. **33**, 765-921 (2004)
- [27] Whitehead, C., Pournasr, H., Bruce, M., Cai, H., Kohel, J., Layne, W. & Keto, J. Deactivation of two-photon excited Xe (5 p 56 p, 6 p', 7 p) and Kr (4 p 55 p) in xenon and krypton. *The Journal Of Chemical Physics*. **102**, 1965-1980 (1995)
- [28] Xia, T., Morgan, S., Jau, Y. & Happer, W. Polarization and hyperfine transitions of metastable Xe 129 in discharge cells. *Physical Review A*. **81**, 033419 (2010)
- [29] Raymond, T., Böwering, N., Kuo, C. & Keto, J. Two-photon laser spectroscopy of xenon collision pairs. *Physical Review A*. **29**, 721 (1984)
- [30] Kröll, S. & Bischel, W. Two-photon absorption and photoionization cross-section measurements in the 5 p 5 6p configuration of xenon. *Physical Review A*. **41**, 1340 (1990)
- [31] Liu, T., Schnabel, A., Voigt, J., Sun, Z. & Li, L. A three-step model for optimizing coil spacings inside cuboid-shaped magnetic shields. *AIP Advances*. **10** (2020)
- [32] Sayama, S. & Ohtsu, M. Tunable UV CW generation at 276 nm wavelength by frequency conversion of laser diodes. *Optics Communications*. **145**, 95-97 (1998)
- [33] Burkley, Z., Brandt, A., Rasor, C., Cooper, S. & Yost, D. Highly coherent, watt-level deep-UV radiation via a frequency-quadrupled Yb-fiber laser system. *Applied Optics*. **58**, 1657-1661 (2019)
- [34] Fortier, T. & Baumann, E. 20 years of developments in optical frequency comb technology and applications. *Communications Physics*. **2**, 153 (2019)
- [35] Yang, K., Li, W., Shen, X., Bai, D., Zhao, J., Yan, M. & Zeng, H. Ultraviolet frequency comb generation by frequency quadrupling a high-power fiber amplifier. *CLEO: Science And Innovations*. pp. CM4I-3 (2013)
- [36] ShestaeV, E., Hädrich, S., Walther, N., Eidam, T., Klenke, A., Seres, I., Bengery, Z., Jójárt, P., Várallyay, Z., Börzsönyi, Á. & Others Carrier-envelope offset stable, coherently combined ytterbium-doped fiber CPA delivering 1 kW of average power. *Optics Letters*. **45**, 6350-6353 (2020)
- [37] Müller, M., Aleshire, C., Klenke, A., Haddad, E., Légaré, F., Tünnermann, A. & Limpert, J. 10.4 kW coherently combined ultrafast fiber laser. *Optics Letters*. **45**, 3083-3086 (2020)
- [38] Rothhardt, J., Rothhardt, C., Müller, M., Klenke, A., Kienel, M., Demmler, S., Elsmann, T., Rothhardt, M., Limpert, J. & Tünnermann, A. 100 W average power femtosecond laser at 343 nm. *Optics Letters*. **41**, 1885-1888 (2016)
- [39] Baklanov, E. & Chebotaev, V. Two-photon absorption of ultrashort pulses in a gas. *Soviet Journal Of Quantum Electronics*. **7**, 1252 (1977)
- [40] Piqué, N. & Hänsch, T. Frequency comb spectroscopy. *Nature Photonics*. **13**, 146-157 (2019)
- [41] Bartels, A., Heinecke, D. & Diddams, S. 10-GHz self-referenced optical frequency comb. *Science*. **326**, 681-681 (2009)
- [42] Kippenberg, T., Holzwarth, R. & Diddams, S. Microresonator-based optical frequency combs. *Science*. **332**, 555-559 (2011)
- [43] Agrawal, G. Nonlinear Fiber Optics. (Elsevier Science, 2013)
- [44] Zervas, M. & Codemard, C. High power fiber lasers: a review. *IEEE Journal Of Selected Topics In Quantum Electronics*. **20**, 219-241 (2014)
- [45] Limpert, J., Roser, F., Schreiber, T. & Tünnermann, A. High-power ultrafast fiber laser systems. *IEEE Journal Of Selected Topics In Quantum Electronics*. **12**, 233-244 (2006)
- [46] Steinmetz, T., Wilken, T., Araujo-Hauck, C., Holzwarth, R., Hänsch, T. & Udem, T. Fabry-Pérot filter cavities for wide-spaced frequency combs with large spectral bandwidth. *Applied Physics B*. **96** pp. 251-256 (2009)
- [47] Mildner, J., Meiners-Hagen, K. & Pollinger, F. Dual-frequency comb generation with differing GHz repetition rates by parallel Fabry-Pérot cavity filtering of a single broadband frequency comb source. *Measurement Science And Technology*. **27**, 074011 (2016)
- [48] Lesundak, A., Smid, R., Voigt, D., Cizek, M., Berg, S. & Cip, O. Repetition rate multiplication of a femtosecond frequency comb. *Photonics, Devices, And Systems VI*. **9450** pp. 404-412 (2015)
- [49] Hou, L., Han, H., Zhang, L., Pang, L. & Wei, Z. An Yb-fiber laser comb with mode spacing of higher than 20 GHz by two Fabry-Pérot cavities. *Conference On Lasers And Electro-Optics/Pacific Rim*. pp. 25F2.4 (2015)
- [50] Cerez, P., Giordano, V., Dimarcq, N., Hamel, A. & Théobald, G. Accurate measurement of the fluorescence collection efficiency in a light-atom interaction experiment. *Measurement Science And Technology*. **1**, 1106 (1990)
- [51] Swallows, M., Loftus, T., Griffith, W., Heckel, B., Fortson, E. & Romalis, M. Techniques used to search for a permanent electric dipole moment of the 199 Hg atom and the implications for CP violation. *Physical Review A*. **87**, 012102 (2013)